Muffin-tin potentials in EXAFS analysis

B. Ravel*

National Institute of Standards and Technology, Gaithersburg, MD 20899, USA.
*Correspondence e-mail: bravel@bnl.gov

Muffin-tin potentials are the standard tool for calculating the potential surface of a cluster of atoms for use in the analysis of extended X-ray absorption fine-structure (EXAFS) data. The set of Cartesian coordinates used to define the positions of atoms in the cluster and to calculate the muffin-tin potentials is commonly also used to enumerate the scattering paths used in the EXAFS data analysis. In this paper, it is shown that these muffin-tin potentials are sufficiently robust to be used to examine quantitatively contributions to the EXAFS data from scattering geometries not represented in the original cluster.

1. Overview of muffin-tin potentials

In the decade from the mid-1980s to the mid-1990s, the main components of an analytical theory of extended X-ray absorption fine structure (EXAFS) were finalized and put into the form of user-oriented software. Three efforts from that era gained wide user bases and remain in use today (Gurman *et al.*, 1986; Filipponi *et al.*, 1995; Zabinsky *et al.*, 1995). These three efforts have much in common, each breaking the problem into three components, (1) calculation of the potential surface of a cluster of atoms, (2) enumeration of single scattering (SS) and multiple scattering (MS) configurations in the cluster and (3) calculation of the complex scattering function for configuration.

While this manuscript makes specific reference to *FEFF* (Zabinsky *et al.*, 1995), all three of the programs, in fact, use the same basic scheme for the calculation of the potential surface of the cluster, the *muffin-tin potential* model. In the muffin-tin (MT) model (Slater, 1937), neutral atoms (Anku-dinov *et al.*, 1996) are placed at positions indicated by a list of Cartesian coordinates. This cluster is typically a few tens or hundreds of atoms and has no requirement of symmetry or periodicity. Each atom in the cluster, then, is defined by its three Cartesian coordinates and the Z number of its atomic species.

For most real materials, the coordinates of the atoms in the cluster result in interatomic distances that are shorter than the radii of the neutral atoms. Overlap of atoms is handled using some variation of the Mattheiss prescription (Mattheiss, 1964), in which Wigner–Seitz cells are created about each position in the cluster, then spheres are inscribed in the cells. These MT spheres are, in most cases, smaller than the neutral atom spheres, as shown schematically in Fig. 1. The MT spheres necessarily contain less electron charge than the larger neutral atom spheres. This excess charge is placed uniformly throughout the volume occupied by the cluster.

From these slightly charged spheres, the complex photo-electron scattering functions are computed using the default models in *FEFF* for the atomic potentials and the energy-
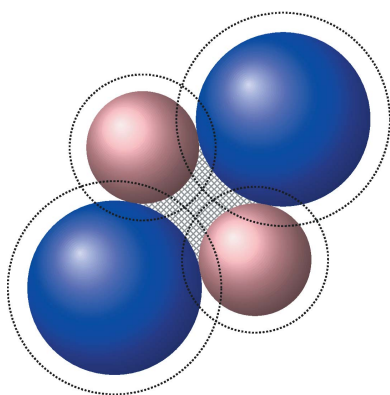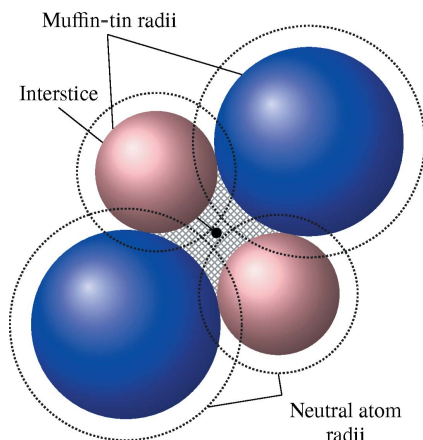
Figure 1
Schematic of the construction of the muffin-tin potential.

dependent Hedin–Lundqvist (Zabinsky *et al.*, 1995) self-energy. A majority of the EXAFS analysis in the literature has used this same potential model.

It is, perhaps, surprising that this model is so successful. This simple construction contains little chemistry. There is no mechanism to move charge between spheres, as expected of ionic bonding. Nor is there any concept of a covalent bond, which would imply excess charge density in certain directions. While both of those shortcomings can be improved upon in the theory, EXAFS analysis is regularly made without either improvement while still producing useful, defensible results. This is because the analysis of the EXAFS data typically begins about 3 Å^{-1}, or about 35 eV, above the absorption edge. In the EXAFS region, the photoelectron has high kinetic energy, thus is rather insensitive to the details of the potential surface.

2. Using muffin-tin potentials

Once the MT potentials are calculated and the paths are enumerated (Rehr *et al.*, 1992), the signal for each scattering contribution is computed for use in the EXAFS equation,

$$\chi_\Gamma(k) = \frac{NS_0^2 F_\Gamma(k) \exp(-2k^2\sigma_\Gamma^2) \exp[-2R_\Gamma/\lambda(k)]}{2kR_\Gamma^2}$$
$$\times \sin\left[2kR_\Gamma + \delta_\Gamma(k)\right]. \qquad (1)$$

Here, Γ is an index counting over all scattering paths considered in the fit. $F_\Gamma(k)$ and $\delta_\Gamma(k)$ are the amplitude and phase of the photoelectron scattering function as computed for scattering paths of any order using the MT potentials and the details of the individual scattering geometries.

The remaining terms – N, the path degeneracy; S_0^2, the passive electron reduction factor (Li *et al.*, 1995); R, the scattering path length; and σ^2, the mean square variation in scattering path length – are all parameterized using the variables of the fit. Additionally, an energy shift parameter, E_0, is used to align the zero of photoelectron wavenumber k in theory and data. Finally, $\lambda(k)$, the photoelectron mean free path, is also provided by the theory software. All paths used in the analysis are then summed,

$$\chi_{\text{theory}}(k) = \sum_\Gamma \chi_\Gamma(k), \qquad (2)$$

and compared with the measured $\chi(k)$.

In common practice, the list of Cartesian coordinates and Z numbers are used both for the calculation of the MT potentials and for the enumeration (Zabinsky *et al.*, 1995) of scattering contributions. In fact, MT construction and path enumeration are two separate chores that need not use the same input data. In this manuscript, a real data analysis problem is presented as an example of a situation where treating these two chores separately is fruitful.

3. Experimental methods

Polycrystalline $LaNiO_3$ was prepared by the citrate gel method described by Marcilly *et al.* (1970). Here, 0.01 mmol of $La(CH_3CO_2)_3 \cdot H_2O$ and 0.01 mmol of $Ni(CH_3CO_2)_2 \cdot 4H_2O$ were dissolved in 20 ml of deionized water under stirring. To this solution was added 0.04 mmol of citric acid monohydrate dissolved in 5 ml deionized water, leading to the formation of a white precipitate. The pH was adjusted to circumneutral by dropwise addition of ammonium hydroxide (~30% NH_3 basis) resulting in dissolution of the precipitate. The deep-green solution was evaporated at 343 K to form a rigid gel. The recovered gel was decomposed by heating at 523 K for 2.5 h in air to yield an amorphous precursor. X-ray powder diffraction demonstrated formation of single phase $LaNiO_3$ (black) after heating the amorphous precursors at 1173 K for 36 h under flowing oxygen. The mean particle size of the $LaNiO_3$ powder was estimated as 0.5 μm by scanning electron microscopy. The phase purity of the $LaNiO_3$ powder was verified by X-ray powder diffraction. See the supporting information for details about the preparation of the NiO sample.

A sample of $LaNiO_3$ was prepared for X-ray absorption spectroscopy (XAS) measurements by dispersing enough fine powder in polyethylene glycol to make an appropriate sample for the transmission XAS measurement. A pellet was then formed in a hydraulic press.

XAS data at the Ni K-edge (8333 eV) were measured at beamline X23A2 at the National Synchrotron Light Source at Brookhaven National Laboratory in New York, USA. This is an unfocused bend-magnet beamline using a Si(311) monochromator of a fixed-exit Golovchenko–Cowan (Golovchenko *et al.*, 1981) design. Harmonic rejection was made by a single bounce, flat, Rh-coated mirror. A nitrogen-filled ionization chamber was used to measure the incident and transmitted intensities as well as the intensity passing through a Ni foil used as a reference for energy alignment. There were $\sim 10^9$ photons s^{-1} in a spot of 5 mm in the horizontal and 0.5 mm in the vertical directions. At this low flux density, radiation-induced changes in speciation are not observed.

4. Analysis of LaNiO$_3$ data

To begin, the $LaNiO_3$ data were analyzed starting with its known crystal structures. $LaNiO_3$ crystallizes in a rhombohe-
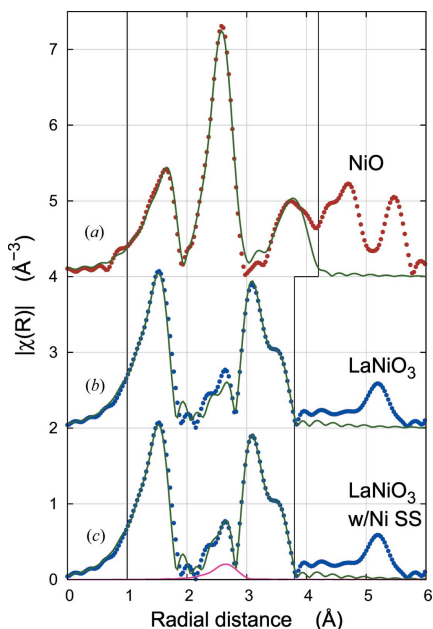
Figure 2
(*a*) Fit to a NiO (brown dots) standard using a simple fitting model based on its cubic halite structure. (*b*) Fit to LaNiO$_3$ (blue dots) using the known rhombohedral structure and the simple model described in the text. (*c*) Fit to the LaNiO$_3$ with the addition of a Ni SS path (pink) as described in the text. The solid green lines are the best fits in each case. The vertical lines represent the ranges over which the fits were evaluated.

Table 1
Results of the fits discussed in the text.

1σ uncertainties, calculated as the diagonal elements of the covariance matrix of the fit, are given in parentheses. Only the portion of the NiO fit immediately relevant to the LaNiO$_3$ analysis is shown, see the supporting information for more information about the NiO fit.

	LaNiO$_3$	With SS path	NiO
S_0^2	0.72 (5)	0.72 (4)	
E_0	−3.05 (57) eV	−3.18 (54) eV	
α	−0.002 (1)	−0.002 (1)	
σ_O^2	0.00307 (81) Å^2	0.00305 (77) Å^2	
σ_{La}^2	0.00569 (59) Å^2	0.00579 (59) Å^2	
σ_{Ni}^2	0.00537 (80) Å^2	0.00538 (76) Å^2	
N:Ni		0.80 (45)	12
R:Ni		3.003 (105) Å	2.951 (4) Å
σ^2:Ni		$\equiv \sigma_{Ni}^2$	0.00539 (56) Å^2

dral modification of the perovskite structure (García-Muñoz *et al.*, 1992). This small rhombohedral distortion results in a splitting of the second shell La scatterers into a group of two La atoms at 3.29 Å and a group of six at 3.34 Å, while the first and third shells are unsplit with six O atoms at 1.93 Å and six Ni atoms at 3.84 Å. The variables of the fit included parameters for S_0^2 and E_0 as well as σ^2 for the O, La and Ni single-scattering paths. Because the distortion away from the cubic perovskite structure is small, the approximation of a fitted isotropic expansion coefficient α is used in each path to compute the change in R as $\Delta R = \alpha R_0$, where R_0 is the path length in the *FEFF* calculation. Various MS paths are included in the fit and parameterized without introducing any new fitting variables. Analysis was performed using the *ARTEMIS* program (Ravel & Newville, 2005; Newville, 2001). This simple model yields a reasonably good fit as seen in Fig. 2(*b*). All parameters yield reasonable values, as seen in the left-hand column of Table 1. Still, there is significant misfit in the region from 2.2 Å to 2.8 Å, a region dominated in the LaNiO$_3$ structure by single scattering from the La atoms.

This sample, then, represents a common situation encountered in the course of EXAFS analysis. The fit is mostly reasonable, but there is something obviously missing. The point of this manuscript is to present a powerful, flexible tool for solving an analysis challenge like this.

5. Addition of a Ni SS path

The fit shown in Fig. 2(*b*) uses *all* of the paths in the LaNiO$_3$ structure with path lengths of 3.87 Å or less. There is nothing

from the LaNiO$_3$ structure not included in the fit that can contribute the additional spectral weight in the region from 2.2 Å to 2.8 Å. The check for phase purity described in §3 was made by X-ray diffraction. Only the *diffracting* portion of the sample is necessarily pure LaNiO$_3$. There is a possibility that some Ni could be contained in a poorly diffracting oxide that may be nanoscale or amorphous. The NiO data shown in Fig. 2(*a*) supports this assumption – the large contribution from the second shell Ni scatterer in NiO is at just the right location to account for the missing spectral weight in the 2.2 Å to 2.8 Å region.

As part of the potentials calculation for LaNiO$_3$, an MT potential for Ni was calculated. However, there are no Ni scatterers in the 2.2 Å to 2.8 Å range in the LaNiO$_3$ structure. In *FEFF*, the part of the program that performs path enumeration writes a file called `paths.dat`. This is a plain text file that, for each scattering path, has a paragraph which gives the Cartesian coordinates of the atoms in that path. This file, along with the information about the potentials, is used by the part of the program that generates the complex scattering functions for use in the EXAFS equation.

To investigate the prospect of a Ni scatterer, a `paths.dat` file is created with a single paragraph describing a SS path with the Ni absorber and a Ni scatterer at the position (0, 0, 2.97). *FEFF* uses the Ni MT potential from the LaNiO$_3$ calculation and this specially crafted `paths.dat` file to generate the Ni SS contribution to the EXAFS at that distance.

The result of a fit using this specially crafted SS path is shown in Fig. 2(*c*) with the contribution from that path shown in pink. The addition of this SS path resolves most of the misfit in the 2.2 Å to 2.8 Å region. This path was parameterized with its own fitting variables, see the third column of Table 1, for N, ΔR and σ^2. The S_0^2 and E_0 from the LaNiO$_3$ portion of the fitting model were used for this path. The parameters related to LaNiO$_3$ change only slightly with the addition of the Ni SS path.

Comparing the result for N with the 12 Ni neighbors in bulk NiO, we can approximate the fraction of Ni atoms in the poorly diffracting oxide phase as 6.3 (3.5)%. The R value is consistent within error bars with the value from the analysis of NiO. When the σ^2 parameter for the Ni SS path was floated

freely, the fit proved unstable, yielding ill-defined values for all three parameters. This is likely because of the small contribution of the Ni SS path to the entire EXAFS spectrum. Noting that the σ^2 for the Ni second neighbor in NiO is very close to the σ^2 for the Ni scatterer in LaNiO$_3$, the σ^2 for the Ni SS path was constrained to that value. This stabilized the fit, resulting in the N and R values reported in Table 1.

While adding the Ni SS path certainly does make the fitted spectrum look more like the data, the fit in Fig. 2(c) is defensible not because it is closer to the data than in Fig. 2(b) but for reasons of chemistry and statistics. The assumption that an amorphous metal oxide might precipitate during sample preparation is both reasonable and common when using sol–gel synthesis. Further, as discussed in the supporting information, the addition of the N and R fitting parameters improved the quality of fit, as seen by a reduction in the χ_ν^2 fitting metric. This result is chemically and statistically defensible and not merely an *ad hoc* alteration of a fitting model.

6. Discussion

To understand why this method of constructing a SS path works so well in the analysis, consider the nature of the MT potential. The main parameters of the potential are the atomic species of the scatterer and the size of the MT sphere. In the NiO *FEFF* calculation, the MT radius of the Ni^{2+} ion is 1.154 Å, for the Ni^{3+} in the LaNiO$_3$ *FEFF* calculation it is 1.034 Å. In fact, any real crystal containing Ni and O will have a nearest neighbor around 2 Å, resulting in a similar value for the Ni MT radius.

In Fig. 3, the contribution from a single Ni atom in the second shell of NiO (blue) is compared with the contribution from the Ni SS path computed using the MT potentials from the LaNiO$_3$ calculation (red). Despite the difference in MT radii, the computed $\chi(k)$ are nearly identical, with most of the difference in k being below the range of the Fourier transform. The substantial advantage of computing a scatterer at about the right distance out-weighs the small error introduced by the slightly incorrect MT radius. Fitting the LaNiO$_3$ data using the second shell of NiO in place of the Ni SS path results in a nearly identical fit. This is shown in detail in the supporting information.

In the *ARTEMIS* program, the implementation of the SS path requires the user to select a scatterer species from a *FEFF* calculation that has already been run and to specify a distance between the absorber and the scatterer.

One possible counterpoint to this presentation is that NiO is a well known, readily available standard. It is easy to run *FEFF* on the known NiO structure (Wyckoff, 1963) and to use the Ni SS path from that calculation in the fit to the LaNiO$_3$ data. While that would be a fine strategy in this case, there are several reasons the method presented here – reusing MT potentials from an existing calculation with specially crafted scattering geometries – is attractive.

Once implemented in a data analysis program, this way of making scattering contributions provides a quick, convenient
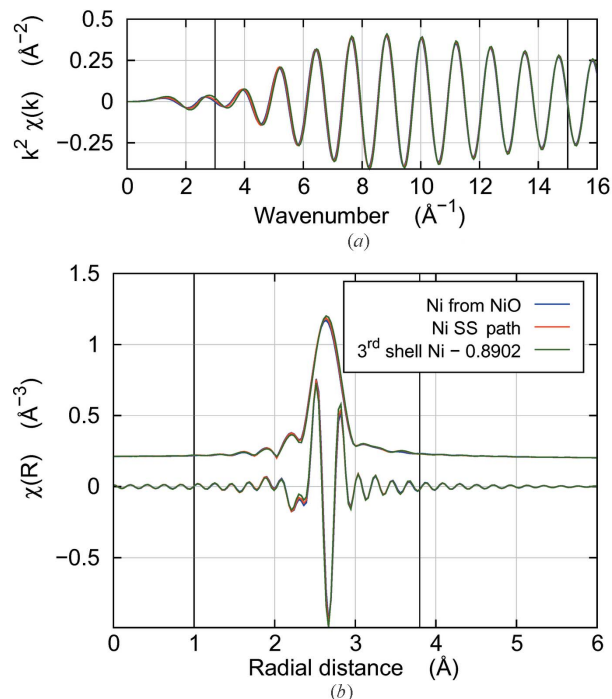

Figure 3
(a) A single Ni atom at 2.9475 Å, computed using the NiO MT potentials (blue) and the LaNiO$_3$ MT potentials (red), as $\chi(k)$. The third trace (green) shows the third shell Ni scatterer from LaNiO$_3$ shifted by 0.8902 Å to 2.9475 Å. (b) The magnitude and real part of the Fourier transforms of those three calculations. The vertical black lines represent the Fourier transform and fitting ranges used in the analysis of the data from the mixed sample.

way to test specific scatterers at specific distances against the data being analyzed. It allows for the investigation of absorber–scatterer pairs at distances that might be hard to find in a well characterized standard or an established crystal structure.

A second possible counterpoint is that a large ΔR can be applied to the Ni path at 3.838 Å in the LaNiO$_3$ structure to shift it to a position near 3 Å. This is shown as the green trace in Fig. 3. This is substantively similar to the calculation using the NiO MT potentials, but with larger (albeit still small) deviation below 5 Å^{-1} resulting from the R dependence of the computation of the complex scattering function from the MT potentials. Whether the approach of applying a large ΔR is more or less complicated than the path construction suggested in this manuscript is an implementation detail of the data analysis software.

Extending this method to MS is a trivial extension of the procedure described in §5. Any MS path could be computed by providing either a set of Cartesian coordinates or a set of lengths and scattering angles. Consider a material for which nominally collinear MS paths can deviate from collinearity when lattice distortions are considered in a fitting model. Examples of this sort of analysis in the literature tend to use approximations to the effect of a small deviation from collinearity on these important MS paths. One such example is given by Frenkel *et al.* (1996). Constructing MS paths in this way would be a more accurate, low-overhead mechanism for

incorporating the effect of a variable scattering angle in the EXAFS fitting loop.

References

Ankudinov, A., Zabinsky, S. & Rehr, J. (1996). *Comput. Phys. Commun.* **98**, 359–364.

Filipponi, A., Di Cicco, A. & Natoli, C. R. (1995). *Phys. Rev. B*, **52**, 15122–15134.

Frenkel, A., Stern, E., Voronel, A. & Heald, S. (1996). *Solid State Commun.* **99**, 67–71.

García-Muñoz, J. L., Rodríguez-Carvajal, J., Lacorre, P. & Torrance, J. B. (1992). *Phys. Rev. B*, **46**, 4414–4425.

Golovchenko, J., Levesque, R. A. & Cowan, P. L. (1981). *Rev. Sci. Instrum.* **52**, 509–516.

Gurman, S., Binsted, N. & Ross, I. (1986). *J. Phys. C*, **19**, 1845–1861.

Li, G., Bridges, F. & Booth, C. (1995). *Phys. Rev. B*, **52**, 6332–6348.

Marcilly, C., Courty, P. & Delmon, B. (1970). *J. Am. Ceram. Soc.* **53**, 56–57.

Mattheiss, L. F. (1964). *Phys. Rev.* **133**, A1399–A1403.

Newville, M. (2001). *J. Synchrotron Rad.* **8**, 322–324.

Ravel, B. & Newville, M. (2005). *J. Synchrotron Rad.* **12**, 537–541.

Rehr, J. J., Albers, R. C. & Zabinsky, S. I. (1992). *Phys. Rev. Lett.* **69**, 3397–3400.

Slater, J. C. (1937). *Phys. Rev.* **51**, 846–851.

Wyckoff, R. (1963). *Crystal Structures.* New York: Wiley.

Zabinsky, S. I., Rehr, J. J., Ankudinov, A., Albers, R. C. & Eller, M. J. (1995). *Phys. Rev. B*, **52**, 2995–3009.